Journal of *Marine Science and Engineering*

MDPI

Article

Research on Prediction Method for Heave Motion of Cylindrical FPSO Based on Viscous Correction

Shenglei Fu [1], Wei Gao [1], Yuanfang Li [1], Ying Xie [2,3,4], Tianqi Wang [2,3,4] and Chen An [2,3,4,*]

[1] CNOOC Research Institute Co., Ltd., Beijing 100028, China; fushl5@cnooc.com.cn (S.F.); gaowei46@cnooc.com.cn (W.G.); liyf71@cnooc.com.cn (Y.L.)
[2] College of Safety and Ocean Engineering, China University of Petroleum-Beijing, Beijing 102249, China; 2023211008@student.cup.edu.cn (Y.X.); 2022310508@student.cup.edu.cn (T.W.)
[3] Key Laboratory of Oil and Gas Safety and Emergency Technology, Ministry of Emergency Management, Beijing 102249, China
[4] Key Laboratory of Oil and Gas Production Equipment Quality Inspection and Health Diagnosis, State Administration for Market Regulation, Beijing 102249, China
* Correspondence: anchen@cup.edu.cn

Abstract

Cylindrical floating production storage and offloading (FPSO) units represent a new core asset in offshore oil exploration and development, where their stability and safety under complex sea conditions are critical. The design of their large waterline surface and the fluid resonance effect in the moonpool result in highly complex heave characteristics that are difficult to predict accurately. This paper implements and refines an iterative viscous-damping correction framework to enhance the motion response analysis of a moonpool-equipped cylindrical FPSO. Initially, the platform's motion is captured using ANSYS AQWA and then utilized as a forced-motion input for ANSYS Fluent to simulate the viscous flow field. The equivalent viscous damping coefficients are extracted from the dynamic equilibrium of the drag response and fed back into the potential flow solver. This process is iterated until the heave response achieves convergence, explicitly accounting for the nonlinear dependency of damping on motion amplitude. For regular waves with headings of 0° and 90°, the converged heave damping coefficients were 1.533×10^7 and 2.226×10^7 N·s/m, respectively, corresponding to a dimensionless damping coefficient $C_d \approx 0.67$ in both cases. In the time domain under the design sea state, the predicted heave amplitude decreased by approximately 50% compared with the uncorrected potential-flow result. Results indicate that the viscous damping correction method significantly reduces the platform's response amplitude operator (RAO), drag, and heave response under, effectively mitigating excessive responses caused by the moonpool effect. This study provides a more reliable framework for the structural design and mooring configuration of cylindrical FPSOs.

Keywords: cylindrical FPSO; moonpool; viscous damping; heave response; correction method

Check for updates

Academic Editor: Atilla Incecik

Received: 22 January 2026
Revised: 22 February 2026
Accepted: 26 February 2026
Published: 28 February 2026

Copyright: © 2026 by the authors. Licensee MDPI, Basel, Switzerland. This article is an open access article distributed under the terms and conditions of the Creative Commons Attribution (CC BY) license.

1. Introduction

Cylindrical floating production storage and offloading (FPSO) units represent a novel offshore structure type integrating oil and gas extraction, processing, storage, and export functions. For the high efficiency requirement of oil field exploitation, the cylindrical FPSO unit has drawn more attention in recent years for its better sea keeping properties, such as sightly yaw motion, hogging and sagging loads [1–3]. Li et al. [4] showed that for platforms

with identical principal dimensions, the moonpool-equipped platform exhibited markedly better responses in three degrees of freedom—heave, pitch, and roll—than the corresponding platform without a moonpool. However, the large waterline area of such structures can generate significant heave responses in waves, compromising operational efficiency and safety [5,6]. Simultaneously, resonance occurs particularly when incident wave or vessel harmonic motion frequencies approach the moonpool's natural frequency, manifesting as violent piston motion and swaying [7]. These factors collectively render the heave characteristics of moonpool-equipped cylindrical FPSO units complex and challenging to predict accurately.

Due to the viscous effects induced by the water motion inside the moonpool, potential-flow theory has difficulty in accurately predicting the platform responses [8]. Therefore, Computational Fluid Dynamics (CFD) methods are often employed to predict the responses of moonpool-equipped platforms with higher fidelity. Jie et al. [9] simulated the hydrodynamic behaviors of several floating breakwaters with moonpool by the Smoothed Particle Hydrodynamics (SPH) method. The coupled SPH model was validated against physical model tests, showing good agreement with the experimental data, with discrepancies less than 7%. Subsequently, Li et al. [4] developed a coupled framework by integrating the open-source SPH solver DualSPHysics with MoorDyn to simulate wave–structure interaction and the mooring-coupled response of a moonpool-equipped platform. The results also indicate that the platform responses are strongly affected by the incident wave height and the effective length of the moonpool. Nevertheless, fully CFD approaches are computationally demanding and thus inefficient for long-duration time-domain analyses required in engineering practice [10].

Therefore, to calculate the platform response more efficiently and accurately, a method that equates the moonpool viscosity effect to damping has been proposed. Since the added mass and damping during platform motion are closely related to the fluid flow characteristics around the platform, Ji et al. [11] proposed a method for calculating added mass and damping coefficients based on CFD theory. Building upon this method, Yu et al. [12] used Fluent software to establish a three-dimensional numerical tank model. Employing forced heave motion, they calculated the heave damping coefficient and added mass of a cylindrical FPSO unit under different motion parameters. To represent more realistic viscous damping with memory and frequency dependence, fractional viscoelastic formulations provide a promising extension; for example, Pan et al. [13] developed Caputo-based spring-pot models and adopted the L2-1σ discretization to improve numerical accuracy over the Grünwald–Letnikov scheme. In practical applications, the impact of damping on the hydrodynamic characteristics of the platform has attracted attention. Ponnappan et al. [14] systematically compared the influence of different moonpool cross-sectional shapes on platform hydrostatic resistance through numerical simulations. Lee et al. [15] improved moonpool configurations using CFD methods, achieving resistance minimization while maintaining overall moonpool dimensions.

However, these studies mainly focus on resistance rather than motion-response accuracy, and the linkage between damping and the heave RAO—especially in the vicinity of moonpool resonance—has not been fully established. Moreover, viscous damping is often introduced as a one-shot or constant correction, lacking iterative RAO updating and explicit convergence control. This paper proposes a damping iterative model and applies it to the calculation of the motion response of a cylindrical FPSO unit with a moonpool. The main contributions of this study are twofold: (i) an iterative RAO-updating framework in which an equivalent viscous damping term, identified from CFD-based forced-motion resistance, is consistently fed back into the potential-flow solution until a prescribed convergence criterion is satisfied; and (ii) a quantitative assessment of how the viscous-damping

correction alters the predicted heave RAO, with particular emphasis on the vicinity of moonpool resonance. The method was verified by examining the convergence behavior of the iterative RAO updating and by validating the dimensionless damping coefficients derived from the identified equivalent damping against established benchmark ranges and theoretical predictions reported in the literature. Figure 1 summarizes the overall workflow of the proposed iterative viscous-damping correction method.

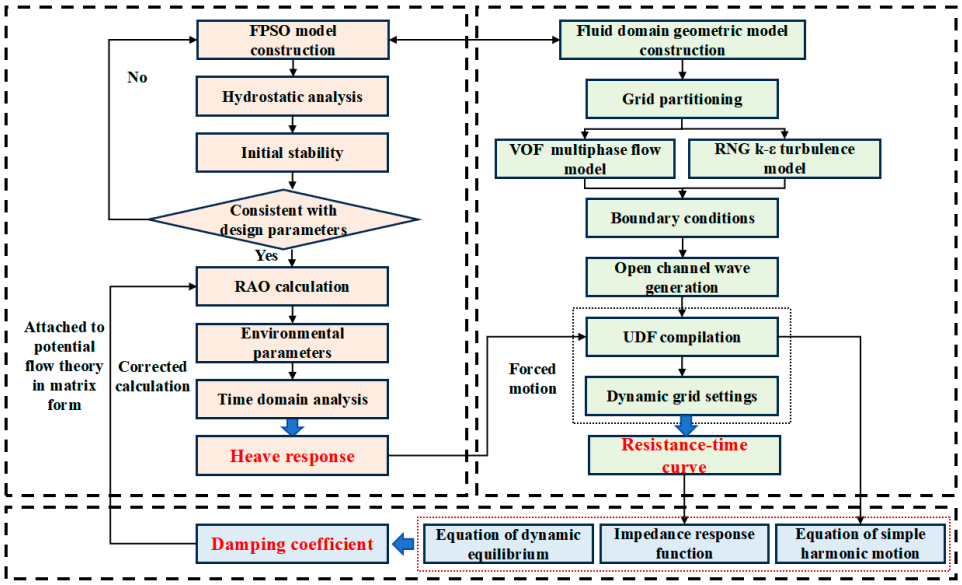


Figure 1. Flowchart of the damping correction method for a cylindrical FPSO unit.

2. Platform Hydrodynamic Characteristics Analysis

2.1. Platform Model and Parameters

In this study, a typical cylindrical FPSO unit was selected as the research object [16]. Its core geometric features are shown in Figure 2: the main structure diameter was 75 m. To suppress hydrodynamic motion response, the bottom buoyancy body extended outward to a diameter of 99 m. The main deck height was 24.5 m, and the upper deck height was 36.5 m. A cylindrical moonpool with a diameter of 25 m was positioned centrally within the main hull. To avoid errors caused by scale effects, subsequent modeling and analysis were based on the actual dimensions of this drilling platform. Key geometric parameters are listed in Table 1, with a structural draft of 15 m.

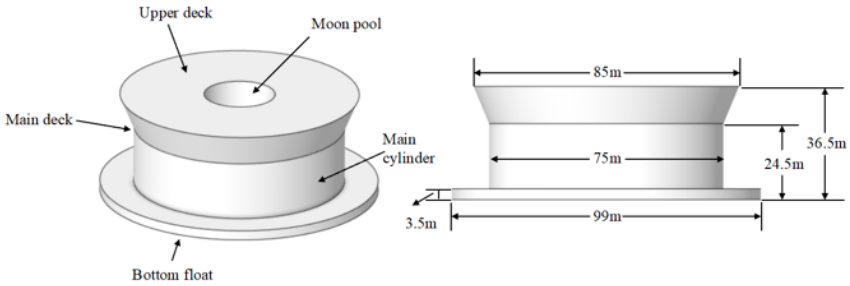


Figure 2. Schematic diagram of the cylindrical FPSO model.

Figure 3 shows the potential flow mesh model of the cylindrical FPSO unit (brown platform in Figure 3) and mooring system (yellow lines in Figure 3) in this study. The mooring system employs a multi-point mooring configuration [17]. Twelve anchor chains are divided into three groups, each containing four chains. The X-direction in Figure 3 is 0°. Specific anchor points and fairlead positions are listed in Table 2. Each anchor chain has a deployed length of 2307 m and a pre-tension of 2018 kN. The platform exhibits high initial

stability, with a waterline area of 3754 m^2 and a displacement volume of 56,995 m^3. In this study, the chain dry weight, equivalent diameter, axial stiffness, and minimum breaking load were 386.9 kg/m, 0.146 m, 1.221×10^6 kN, and 1.85×10^4 kN, respectively.

Table 1. FPSO unit main scale parameter dimensions.

Main Scale Parameters	Symbol	Unit	Physical Dimensions
Body Diameter	DM	m	75.000
Main Deck Height	HM	m	24.500
Bottom Float Diameter	DB	m	99.000
Bottom float height	HB	m	3.500
Upper Deck Height	HUP	m	36.500
Upper Deck Diameter	DUP	m	85.000
Moonpool Radius	r	m	12.500
Draft	T	m	15.000
Center of Gravity Height (from Base Line)	ZG	m	18.556
Weight	G	ton	5.88 × 106
Radius of Gyration	(K_{xx}, K_{yy}, K_{zz})	m	(25, 25, 28.2)
Hydrostatic Stiffness	(C33, C44, C55)	kN/m	(37,742, 13,3671, 133,451)
Natural Period	T_{heave}	s	15.85

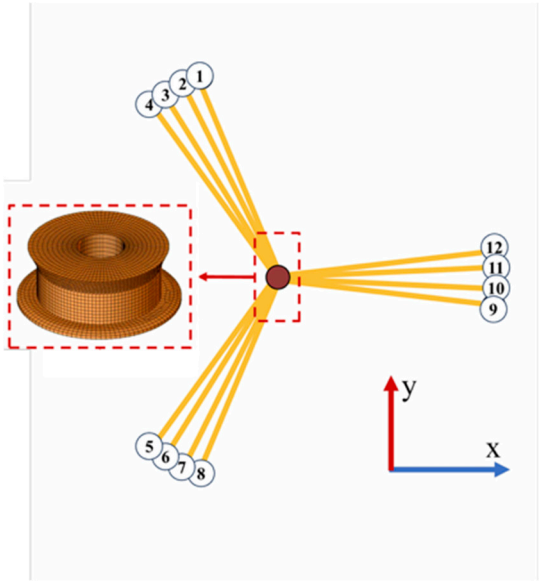


Figure 3. Mesh model of cylinder FPSO unit with a moonpool and mooring system layout.

Table 2. Anchor points and fairlead locations of the mooring system.

No.	Anchor Point			Fairlead		
	X(m)	Y(m)	Z(m)	X(m)	Y(m)	Z(m)
1	1102.3	1436.6	−1500	23.13	30.15	−12.5
2	972.9	1527.2	−1500	20.42	32.05	−12.5
3	836.1	1606.1	−1500	17.55	33.71	−12.5
4	692.9	1672.9	−1500	14.54	35.11	−12.5
5	−1795.2	236.3	−1500	−37.67	−4.96	−12.5
6	−1809	79	−1500	−37.96	1.66	−12.5
7	−1809	−79	−1500	−37.96	−1.66	−12.5
8	−1795.2	−236.3	−1500	−37.67	4.96	−12.5
9	692.9	−1672.9	−1500	14.54	−35.11	−12.5
10	836.1	−1606.1	−1500	17.55	−33.71	−12.5
11	972.9	−1527.2	−1500	20.42	−32.05	−12.5
12	1102.3	−1436.6	−1500	23.13	−30.15	−12.5

2.2. Time-Domain Governing Equations

The time-domain control equation is central to potential flow calculations. In commercial software ANSYS AQWA 2022 R1, wave, current, and wind loads are considered within a single equation of motion. Solving this equation yields the initial heave response of the platform in time-domain analysis, without accounting for viscous effects. This result serves both as a baseline for comparison with corrected outcomes and as the forced motion input for CFD software Fluent 2022 R1.

The time-domain governing equation can be expressed as [8]:

$$(M + m_\infty)\ddot{x}(t) + D\dot{x}(t) + (K + E)x(t) + \int^t h(t-\tau)\dot{x}(\tau)d\tau = q(t, x, \dot{x}) \quad (1)$$

where M denotes the platform mass matrix, m_∞ represents the added mass matrix at infinite wave frequency, K signifies the restoring matrix provided by hydrostatic forces, D indicates the radiative damping matrix, and E denotes the external restoring matrix provided by the mooring lines. $x(t)$, $\dot{x}(t)$, $\ddot{x}(t)$ respectively represent the displacement, velocity, and acceleration vectors. $q(t, x, \dot{x})$ represents the excitation force vector, including wind loads, current loads, first- and second-order wave loads, and the restoring force provided by the mooring system. $h(t)$ is the hysteresis function, defined as:

$$\begin{cases} h(t) = \frac{1}{\pi}\int_0^\infty [d(\omega)\cos\omega\tau - \omega a(\omega)\sin\omega\tau]d\omega \\ a(\omega) = A(\omega) - A_\infty \\ d(\omega) = D(\omega) - D_\infty \end{cases} \quad (2)$$

where D_∞ and A_∞ are the damping and added mass matrices at infinite frequency, respectively.

In this study, the hydrodynamic coefficients used to construct $h(t)$ were evaluated over a prescribed discrete frequency set. The wave- period range was 3.66–62.83 s, with 48 intermediate frequency values. Based on Equations (1) and (2) implemented in ANSYS AQWA, the hydrodynamic performance of the platform was evaluated, and time-domain simulations provided the platform's time histories of motion responses. However, within the potential-flow framework, the viscous damping associated with the moonpool region cannot be captured explicitly. Therefore, CFD calculations were required to quantify the moonpool-induced viscous effects and to update the damping coefficients used in AQWA.

3. Platform Resistance Characteristics Calculation

3.1. Fluid Domain Construction and Mesh Generation

This study employed ANSYS Fluent 2022 R1 software based on CFD methodology to construct the numerical water tank [18] and compute the resistance performance of the cylindrical platform. The determination of computational domain dimensions adheres to two core principles to minimize boundary interference with the core flow field (around the platform and wave field). First, by controlling the width (Y-direction) and depth (Z-direction) of the computational domain, the ratio of the platform's maximum waterline cross-sectional area to the corresponding flow-through area of the basin (i.e., the blockage ratio) is kept below 5%. This effectively suppresses non-physical reflections and blockage effects caused by the sidewalls and bottom surface on the flow. Second, the computational domain possesses sufficient length along the wave propagation direction (X-direction). This ensures that the distance from the wave-generating boundary to the platform, and from the platform to the wave-attenuating boundary, both exceed twice the characteristic wavelength. This provides ample space for wave development, stable propagation, and sufficient attenuation for radiated and diffracted waves generated after passing the platform, thereby avoiding false reflections at the exit boundary.

The established fluid domain model is shown in Figure 4. The fluid domain pool had a length L = 1000 m, width W = 400 m, and height H = 500 m. The cylindrical floating body was placed at the center of the fluid domain, with its center located at the coordinate origin. The distance from the center to both ends of the pool was Lc = 500 m, and the distance from the center to the bottom of the pool was Hc = 200 m. The origin of the global coordinate system (z = 0) was defined at the center of the moonpool's bottom. Based on this, the initial hydrostatic free surface was set at z = 15 m, meaning that the moonpool bottom lay 15 m below the hydrostatic surface—consistent with the target platform's operational draft depth.

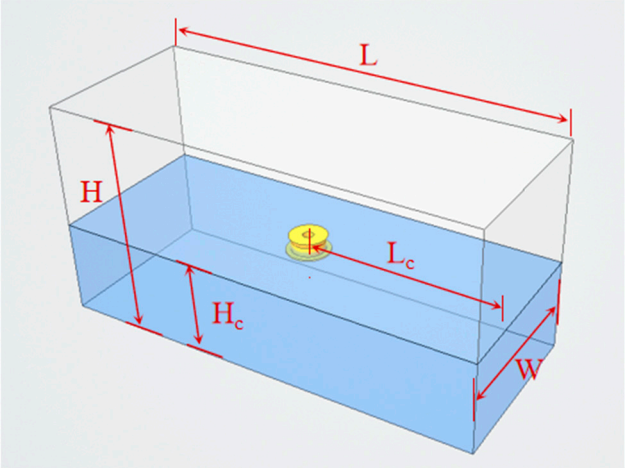


Figure 4. Calculating the size of the pool.

The size and resolution of the mesh directly determine the accuracy of the CFD model. The computational domain is discretized using a hybrid mesh strategy primarily based on hexahedral meshes, ensuring computational accuracy while maintaining computational efficiency. The total mesh comprises 594,567 computational cells and 102,152 nodes. To converge to high-fidelity results, local mesh refinement in regions with drastic gradient changes in physical quantities, such as the free surface, has become a key technique for simulating wave loads on marine structures [19]. Therefore, to accurately capture the surrounding flow field during the heave of the cylindrical floating body, a rectangular local refinement zone was established in the outflow field surrounding the FPSO hull. To ensure numerical stability and waveform accuracy in wave propagation, another rectangular local refinement zone was set up in the free surface region near the waterline. Local refinement was achieved within each refinement zone by employing custom mesh sizes.

The locally refined mesh region spanned 7 m, featuring a boundary layer (expansion layer) on the hull surface. The "Smooth Transition" algorithm was applied with a transition ratio of 0.272, a maximum layer count of 5, and an increment rate of 1.2. The target skewness value in the mesh quality evaluation metrics was set to 0.9. The software automatically optimizes the mesh generation to ensure that the skewness of the vast majority of elements remains below this threshold, meeting the stability requirements of the Fluent solver. Additionally, a minimum edge length of 3.5 m was specified to prevent computational errors caused by excessively elongated elements. The final fluid domain mesh configuration is shown in Figure 5.

3.2. Basic Model and Boundary Wave Generation

Two incompatible fluids—air and water—were present in the simulation analysis. A distinct interface exists between these fluids, and this interface remains in motion throughout the entire computational process. Therefore, the Volume of Fluid (VOF) method was employed to construct the two-phase flow model, capturing the dynamic changes of the free liquid surface. The VOF model tracks the evolution of the gas–liquid interface at the

macroscale by solving the phase fraction transport equation [19]. Under violent heave conditions, the water body within the moonpool exhibits piston-like motion, readily entraining air to form trapped gas pockets or fragmented bubbles. Such phenomena involve complex multiphase interface dynamics. Although the VOF method can theoretically capture such gas–liquid interaction structures, its accuracy is significantly affected by numerical diffusion at the interface and grid resolution. To enhance the accuracy of interface capture, this study aimed to minimize this error through methods such as local grid refinement and the use of geometric reconstruction formats while also conducting grid independence verification.

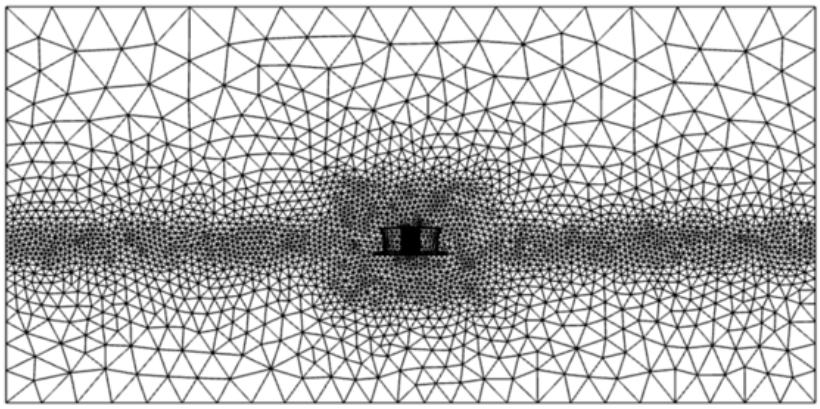


Figure 5. Fluid domain mesh partitioning and refinement.

Simultaneously, to minimize modeling errors as much as possible, the most widely used and recommended RNG k-ε turbulence model was introduced to describe the fluid motion state [20]. This model, derived through renormalization group theory, is better suited for simulating complex vortex structures induced by heave-like oscillations both inside and outside the moonpool. It also exhibits good computational stability and efficiency in long-term transient simulations. Based on the assumption of isotropic vortex viscosity, the model cannot accurately capture local flow field details. However, since the core objective of this study was to extract the macroscopic equivalent damping coefficient, this limitation had minimal impact.

After establishing the model, boundary conditions were applied to the computational domain. The inlet boundary was set as a velocity inlet. To simulate still water conditions, the background velocity at the inlet was set to 0. The turbulence intensity was 5%, with a turbulence viscosity ratio of 10. The corresponding turbulent kinetic energy (k) and turbulent dissipation rate (ε) were 3.75×10^{-7} m^2/s^2 and 2.66×10^{-8} m^2/s^3, respectively. The outlet and top wall were configured as pressure outlets. The top wall was subjected to atmospheric pressure. The "Open Channel" option was enabled for the pressure outlet, with its "Free Surface Level" and "Liquid Level" settings matching those at the inlet, forming an effective wave transmission channel. This configuration combines hydrostatic pressure distribution with density interpolation to physically handle potential backflow in a reasonable manner. Turbulence parameters in the backflow direction remain consistent with those at the inlet. All surfaces (drilling platform surface, computational domain bottom, rear wall, and symmetry plane) were defined as stationary non-slip surfaces. Near-wall turbulence was handled using the standard wall function method, theoretically applicable for target y+ values ranging from $30 < y+ < 300$. By controlling the thickness of the first mesh layer, the actual y+ values on critical walls within the simulation fell within the ideal range of 50 to 150, ensuring the appropriate application of the wall function.

To generate incident waves, ANSYS Fluent's open-channel wave-making function was employed. Regular waves synchronized with the AQWA calculation cycle were applied at the inlet to ensure stability of the numerical water tank environment parameters. This

method offers greater stability and reliability compared to wave-generation approaches based on user-defined function (UDF) compilation and moving mesh technology while also avoiding additional uncertainties [12]. The first-order Airy linear wave theory was selected, with key wave parameters as shown in Table 3: wave height 7.2 m and wavelength 213.62 m. The software automatically calculated the wave kinematic characteristics based on these parameters. Prior to introducing the platform model, wave generation accuracy was validated in an empty water basin. By deploying wave height monitoring points along the propagation direction and comparing the time history of the steady wave surface with theoretical values, it was confirmed that the relative wave height error was less than 3%, the period error was less than 1%, and the phase propagation agreed well with the theory. This indicates that the generated wave field meets the requirements for subsequent analysis. To suppress exit reflections, a 320 m long Eulerian overlapping grid zone was established upstream of the pressure outlet as a wave-dissipating region. Within this zone, the flow equations were progressively attenuated using momentum source terms, effectively dissipating wave energy. Empty basin tests confirmed that the wave reflection coefficient within the domain, estimated using the three-point method, was controlled below 5%, ensuring effective wave dissipation.

Table 3. Open channel wave generation parameters.

Waveform	Period	Wave Length	Wave Height
Airy	11.7 s	213.62 m	7.2 m

To investigate the frequency dependence of the extracted damping coefficient, the system supplemented six sets of non-resonant operating conditions with varying periods (T ranging from 9.75 s to 13.65 s). The computational results are presented in Table 4, revealing a distinct non-monotonic variation of the damping coefficient with wave period: at shorter periods (e.g., T = 9.75 s), the damping coefficient was approximately 1.70×10^7 N· s/m; as the period approached the design condition, the damping first slightly decreased to 1.53×10^7 N·s/m (T = 11.70 s), then exhibited sharp fluctuations as the period continued to increase, reaching 3.76×10^7 N·s/m at T = 13.00 s before abruptly dropping to 4.16×10^6 N·s/m at T = 13.65 s. This trend clearly reveals the strong dependence of viscous damping on excitation frequency, reflecting changes in energy dissipation mechanisms such as vortex shedding and flow separation inside and outside the moonpool at different periods. Although multi-period analysis confirmed the frequency dependence of damping, the primary engineering objective of this study remains focused on determining a high-precision equivalent damping coefficient for the design sea state close to resonance (T = 11.70 s), where motion response is most severe. This condition is central to platform safety assessments, and damping correction at this point holds the greatest practical engineering value.

Table 4. Extraction results of damping coefficients at different periods (H = 7.2 m).

Case ID	Wave Height H (m)	Wave Period T (s)	Relative Change	Damping Coefficient λ (N·s/m)
T-1	7.2	9.75	−16.70%	1.70×10^7
T-2	7.2	10.40	−11.20%	1.26×10^7
T-3	7.2	11.05	−5.60%	8.81×10^6
T-0 (Baseline)	7.2	11.70	0.00%	1.53×10^7
T-4	7.2	12.35	5.60%	9.84×10^6
T-5	7.2	13.00	11.20%	3.76×10^7
T-6	7.2	13.65	16.70%	4.16×10^6

3.3. Sensitivity Analysis

Given the convergence impact of mesh scale and time step on platform hydrodynamic calculations, a corresponding sensitivity analysis was required [21]. Mesh convergence assessment was conducted using refined mesh sizes of 10, 7, and 5 m, yielding platform resistance–time history curves for different mesh refinement levels, as shown in Figure 6. The analysis focused on the steady-state phase after flow fully developed, utilizing data from the final 400 s (approximately 34 motion cycles) of simulation for statistical evaluation.

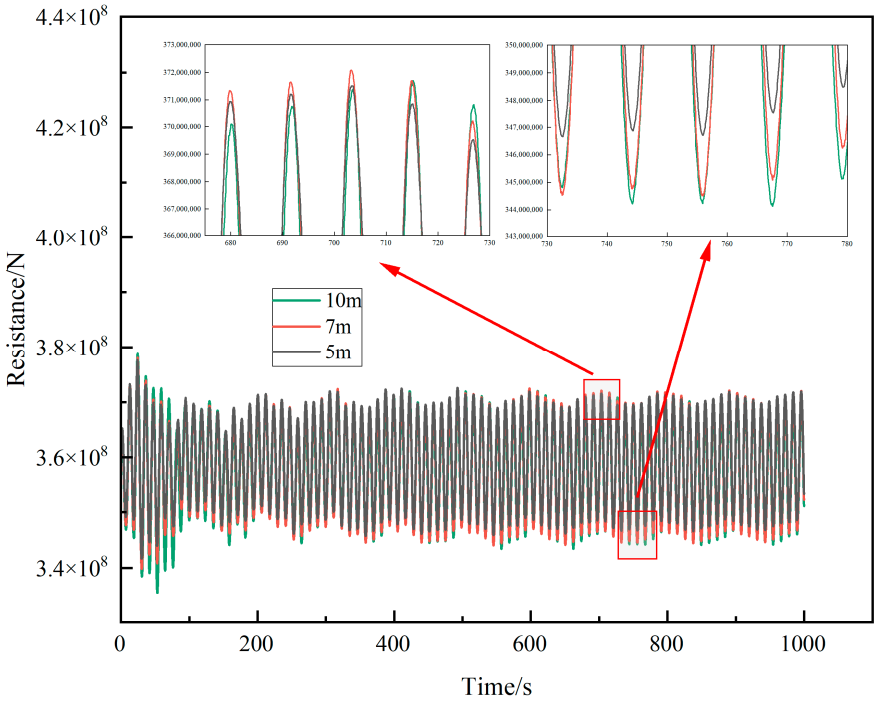


Figure 6. Time course curve of platform resistance with different mesh refinement sizes.

The vertical total resistance time history for the platform during this period was averaged, yielding steady-state average resistances of 3.6661 × 10^8 N (10 m), 3.6528 × 10^8 N (7 m), and 3.6526 × 10^8 N (5 m) for the three grids. The generalized Richardson extrapolation method was employed to calculate the grid convergence index (GCI). The actual convergence order was determined to be $p \approx 2.1$. Accordingly, the GCI for the steady-state average resistance decreased by approximately 5.32% when downscaling from the 10 m grid to the 7 m grid while the GCI decreased to approximately 0.63% when downscaling from the 7 m grid to the 5 m grid. The difference between the 7 m and 5 m grid results was only 0.007%, and the GCI fell below 1%, indicating that the solution for steady-state mean resistance had entered the asymptotic convergence region, with grid discretization errors effectively controlled.

The equivalent linear damping coefficient (λ) obtained from resistance time history inversion is a key output of this study. The damping coefficients obtained from the three mesh calculations were: 1.668 × 10^7 N·s/m (10 m), 1.633 × 10^7 N· s/m (7 m), and 1.629 × 10^7 N· s/m (5 m). A mesh convergence analysis of this damping coefficient revealed a convergence trend consistent with resistance, with a convergence order of $p \approx 2.0$. The GCI estimates for the damping coefficient were approximately 5.3% from the 10 m to 7 m grid and approximately 0.6% from the 7 m to 5 m grid. This confirms that the damping coefficient λ also exhibits good mesh independence.

This validation analysis further extends to other core parameters relied upon by the damping identification method. Calculations indicate that when refining the grid from 7 m to 5 m, the amplitude of the excitation force (F_0) extracted from the resistance spectrum

varied by less than 0.3%, while the phase angle (φ) fluctuated by less than 0.5°, with their respective GCIs remaining below the 1% order of magnitude.

In summary, whether considering the macroscopic steady-state average resistance or the key parameters for damping identification—excitation force amplitude, phase angle, and the final equivalent damping coefficient—the GCI for all of these quantities was below 1% under the 7-m grid scheme. This confirms that solutions for all critical physical quantities have achieved grid independence. Furthermore, regarding computational time, the 5-m mesh calculation took approximately 11 h, while the 7-m mesh calculation took about 6.5 h. Both calculations yielded comparable accuracy, but the 7 m grid computation saved nearly 40% in processing time compared to the 5 m grid. Balancing accuracy requirements and computational cost, a 7 m mesh size was selected for production in this study.

To validate the sensitivity of numerical results to time step size, this study conducted a systematic convergence analysis of time steps. Three time steps were selected for computation: 0.2 s, 0.1 s, and 0.05 s. The time-history curves of the platform's resistance under different time steps are shown in Figure 7. The average resistances during the steady-state phase (simulation's final 400 s) were 3.5785×10^8 N, 3.5827×10^8 N, and 3.5833×10^8 N, respectively. The resistance values exhibited a monotonically converging trend as the step size decreased. The difference between the results for the 0.1 s and 0.05 s step sizes was only 0.017%, indicating that the numerical solution had entered the asymptotic convergence region. To further quantify the discretization error, the GCI was calculated using the generalized Richardson extrapolation method. Under the $\Delta t = 0.1$ s time step scheme, the GCI for steady-state average resistance reached 0.17%, significantly below the 1% threshold (approximately 0.17%). This confirms effective control of temporal discretization errors. Using $\Delta t = 0.1$ s as the computational time step yields steady-state average resistance results with reliable time-step independence.

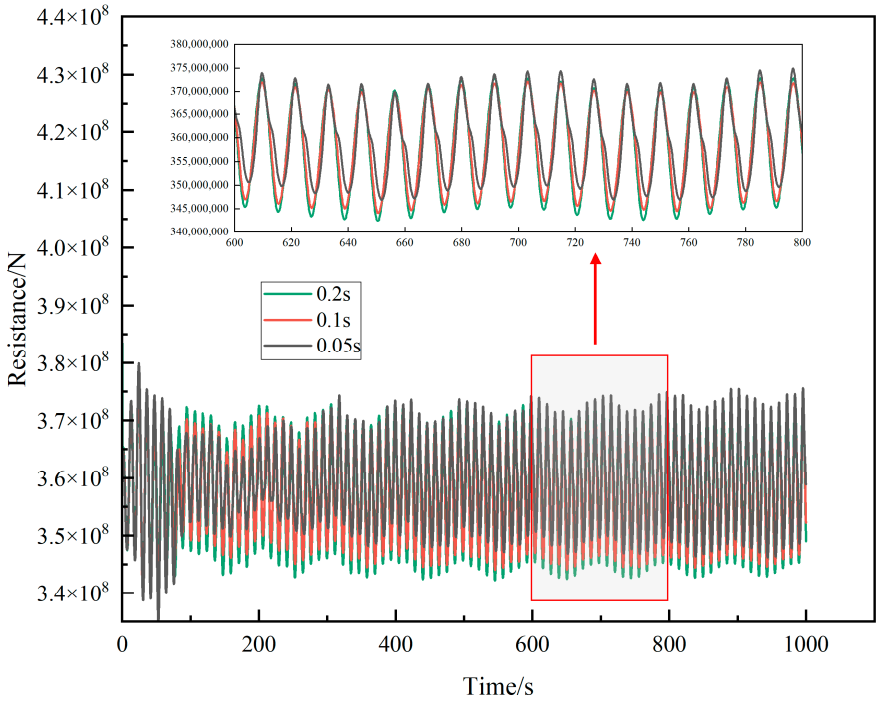


Figure 7. Time course curve of platform resistance at different time steps.

The equivalent damping coefficient λ, obtained from resistance time history inversion, was 1.765×10^7 N·s/m, 1.633×10^7 N·s/m, and 1.628×10^7 N·s/m for the three time steps, respectively. Calculations indicated a convergence order of $p \approx 4.7$, exhibiting high-order convergence characteristics. When the time step was refined from 0.2 s to 0.1 s, the GCI was

approximately 10.5%. Further refinement to 0.05 s significantly reduced the GCI to about 0.41%. This indicates that at the benchmark step size (0.1 s), the temporal discretization error for the damping coefficient is already at an extremely low level (GCI < 0.5%), demonstrating highly reliable step-size independence of the computational results. The variation in phase angle ϕ extracted from the resistance time history was less than 0.5°, with its GCI being of the same order of magnitude as that of the damping coefficient (below 1%).

In summary, under the benchmark time step scheme of Δt = 0.1 s, the GCI for key physical quantities—excitation force, phase angle, and damping coefficient—all fell below 1%. This indicates that the numerical solution exhibits low sensitivity to time steps, with well-controlled discretization errors and reliable computational results. Estimates indicate that at the benchmark step size Δt = 0.1 s, the maximum Courant number was approximately 0.035—well below 1—satisfying computational stability requirements. This step size corresponded to 1/117 of the wave period (T = 11.7 s), meaning each complete wave cycle encompassed over 117 computational time steps, enabling sufficient resolution of dynamic details in wave and platform motion.

Regarding computational efficiency, the Δt = 0.1 s scheme required approximately 6.5 h for a single scenario calculation, whereas the Δt = 0.05 s scheme demanded about 13 h—nearly double the time. Balancing computational accuracy and computational cost, this study ultimately adopted Δt = 0.1 s as the benchmark time step, significantly enhancing computational feasibility while ensuring result reliability.

4. Iterative Solution Method for Heave Damping

This study employed moving mesh technology to achieve forced pure vertical oscillation motion of the platform in still water [22]. Except for the platform's wetted surface, all other boundaries within the computational domain remained stationary. Mesh refinement employed a boundary-distance-based smooth diffusion model (diffusion parameter 1.5) with an AMG solver (CG stabilizer, max iterations 50, convergence tolerance 1×10^{-10}) ensuring quality and stability at each refinement step.

Platform motion is controlled by a data-driven UDF. This UDF reads an externally generated motion time history file precomputed by ANSYS AQWA. It derives the vertical oscillation velocity sequence using the central difference method and assigns the Z-direction velocity to the platform's center of gravity in real-time via linear interpolation at each CFD time step. Simultaneously, the remaining five degrees of freedom are strictly constrained, precisely reproducing pure vertical oscillation motion. This approach ensures high-fidelity motion input and reproducibility of the operating conditions.

The total simulation duration was 1000 s (time step 0.1 s), corresponding to approximately 85.5 motion cycles, providing sufficient time for the flow field inside and outside the moonpool to reach periodic stability. Steady-state determination was based on the vertical resistance time history: when the resistance exhibited a stable, repeating waveform with no further trend changes in its mean value or amplitude, the flow field was considered to have entered periodic steady-state. Analysis indicates that resistance exhibited stable periodicity after approximately 100 s of simulation. Consequently, the final 400 s (spanning over 34 cycles) of steady-state data were selected for extracting all key parameters. This ensured that the analysis results were highly reliable and unaffected by initial transient conditions.

The applied excitation in numerical simulations is pure single-frequency harmonic motion based on AQWA calculations. Based on the equation of simple harmonic motion, the resistance response function and the platform dynamic equilibrium equation can be combined to derive the damping coefficient calculation formula [11]:

$$\lambda = -\frac{F_0 \, sin(\phi)}{A\omega} \tag{3}$$

The damping derivation process assumes linear resistance and single-frequency steady-state response. By performing fast Fourier transform (FFT) analysis on the resistance time history during the steady-state phase of CFD simulation, it was found that over 99.5% of the spectral energy was concentrated at the excitation frequency (corresponding to a period of 11.7 s). This confirms that the resistance response is a quasi-single-frequency signal, validating the validity of the assumption and satisfying the prerequisite conditions for the linear damping extraction method based on Formula (3), where the heave equation of the platform is:

$$a = \mathrm{Acos}(\omega t) \tag{4}$$

where a is the vertical displacement of the platform, A is the amplitude of the floating body motion, and ω is the motion frequency.

The drag response function obtained from CFD numerical simulation is:

$$F = F_0 \cos(\omega t + \phi) \tag{5}$$

where F is the resistance experienced by the floating body, F_0 is the resistance amplitude, and ϕ is the phase difference.

The drag amplitude and phase difference can be extracted from the resistance time history curve using spectral analysis based on FFT. To ensure the reliability of the damping coefficient results, the time window selected for fitting analysis was the stable phase following the complete decay of transient effects in the simulated time history, specifically encompassing all motion cycles within the final 400 s. The heave amplitude, oscillation frequency, drag amplitude, and phase difference are all known. Substituting these values into Equation (3) yields the damping coefficient λ. This method is based on the linear damping assumption. Its approach involves approximating the nonlinear viscous effects caused by parameters such as motion amplitude and wave height in moonpool resonance as an equivalent linear damping coefficient under specific operating conditions. During iterative calculations, these nonlinear parameters are treated as fixed values, thereby determining the "equivalent linearized damping coefficient" corresponding to that operating condition.

In ANSYS AQWA, the preliminarily calculated damping coefficient is introduced via the Additional Damping module. Combined with the configured environmental load parameters, the platform's time-domain response was computed to obtain the corrected heave motion curve. The revised response conditions were rewritten into a UDF file and imported into Fluent. The updated platform motion trajectory was loaded to compute the drag time history curve and extract the corresponding drag response function, enabling further determination of the updated damping coefficient. Iterative updates of the damping coefficient continue until the relative error control criterion is satisfied. Let the damping coefficient obtained at the k-th iteration be $\lambda^{(k)}$. When Equation (6) is satisfied, the iteration is considered converged, completing the vertical damping calculation for the platform.

$$\frac{\left|\lambda^{(k)} - \lambda^{(k-1)}\right|}{\left|\lambda^{(k)}\right|} < 10^{-3} \tag{6}$$

5. Results and Discussion

5.1. Verification of Forced Motion Consistency

To ensure consistency in motion inputs between the AQWA potential flow software and the CFD software Fluent 2022 R1, Figure 8 compares the correspondence between the UDF function curve and the motion curve at different iteration counts, using 0° as an example. The average relative error in the amplitude of the motion curve output by the UDF function compared to AQWA was less than 0.3%. The motion period was

strictly maintained at 11.7 s, fully consistent with the incident wave period. These indicate that excellent data transfer and motion state matching have been achieved between the two software packages. As the iteration count increases, the curve gradually stabilizes, effectively eliminating the initial transient state, and the platform's heave motion enters a steady-state phase. This demonstrates that using the UDF function as forced motion input accurately reproduces AQWA's motion characteristics, laying a reliable foundation for CFD-based damping extraction and correction calculations.

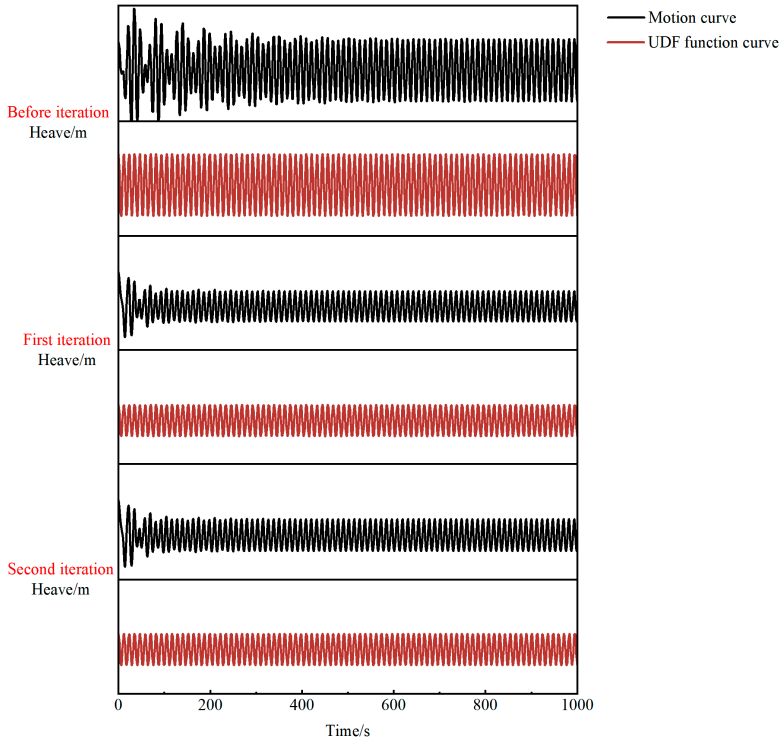


Figure 8. Comparison of UDF function and motion curve (taking 0° incident direction as an example).

5.2. Wave Verification and Monitoring Point Comparison Analysis

To validate the stability and accuracy of the numerical wave field, nine monitoring points were established along the X-axis (x = −150, −75, −50, −10, 0, 10, 50, 75, 150 m). With the center of the wave basin as the origin and the flow velocity direction as the positive direction, wave heights at each point were monitored. As illustrated in Figure 9, the wave height time series curves for monitoring points within the stable segment from 600 s to 800 s at the 0° direction are presented.

Monitoring results indicate that the numerical waves maintained overall stability and sinusoidal characteristics during propagation, validating the rationality of wave generation and propagation settings. Within the moonpool (x = −10 m, 0 m, +10 m), wave heights at monitoring points reached peaks and troughs simultaneously, exhibiting distinct phase synchronization and typical piston-mode characteristics. Further comparison revealed that after waves traverse the moonpool section, wave height amplitudes at downstream monitoring points (x = +50 m, +75 m, +150 m) significantly decreased compared to pre-incidence levels. The wave amplitude ratio between inside and outside the moonpool was 1.56, indicating the moonpool's substantial dissipation of external wave energy. On one hand, the moonpool effect induces overall reciprocating motion of the internal water mass and enhances local viscous dissipation. On the other hand, it attenuates the far-field propagation amplitude of waves [23]. This result reveals the dual influence of the moonpool on both platform motion characteristics and external wave field propagation, providing a physical basis for damping correction and heave motion response analysis.

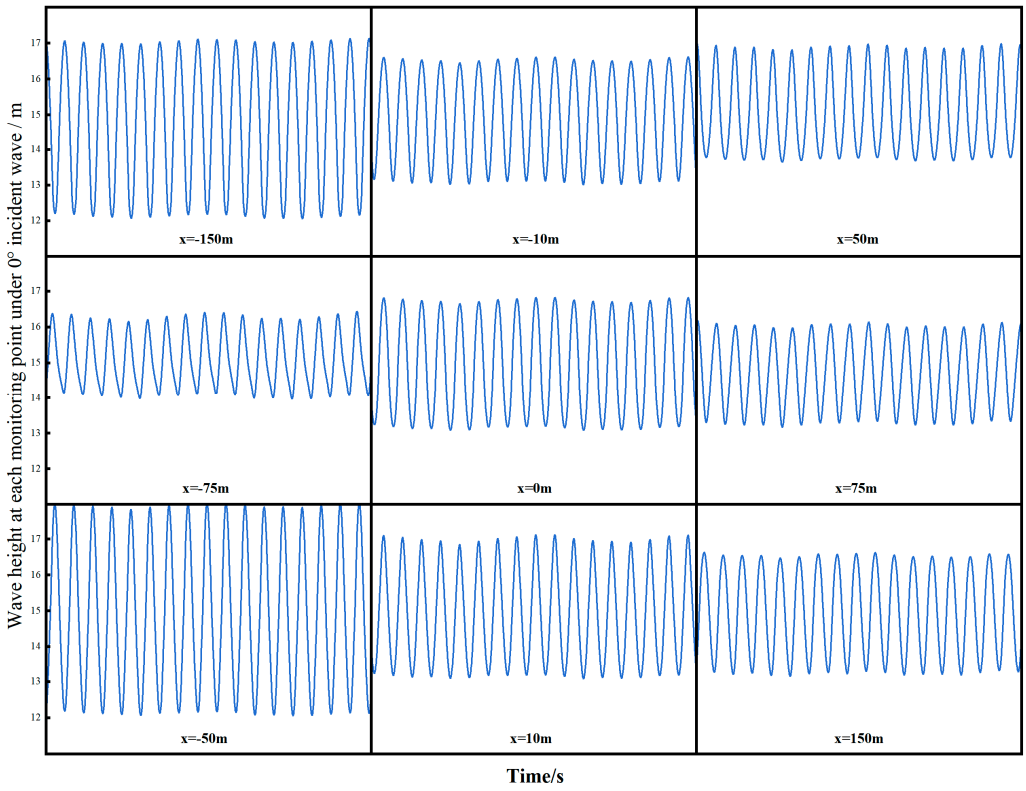


Figure 9. Wave height–time history curves at each monitoring point in the stable section from 600 s to 800 s under a 0° incident wave direction.

5.3. Analysis of Flow Field Distribution Characteristics

Under the 0° incident wave direction, the flow field around the platform exhibited typical moonpool effects. The turbulence intensity distribution is shown in Figure 10a. Its numerical calculation follows the standard definition in the CFD field, defined as the ratio of the root mean square of the turbulent pulsation velocity to the characteristic reference velocity. The reference velocity was selected as the peak velocity of the platform's heave motion. The calculation and extraction location were based on the instantaneous flow field contour plot on the XY plane (i.e., the z = 15 m plane). A distinct wake zone formed at the rear edge of the moonpool, where the highest turbulence intensity peaked at 19.6%. This value significantly exceeded those on both sides of the platform and upstream areas, with the high-turbulence zone extending downstream from the moonpool rear edge.

Both the dynamic pressure distribution (Figure 10b) and velocity field distribution (Figure 10c) exhibited periodic variations along the wave propagation direction. At the moonpool inlet, pressure and velocity significantly increased. The red box marks the peak extraction location, where dynamic pressure reached approximately 2×10^3 Pa and velocity reached about 3.65 m/s. Conversely, a wake zone with lower pressure and velocity formed at the outlet and its downstream region, while relatively high pressure/velocity bands persisted on both sides. This indicates that the interaction between the incident wave and the moonpool structure induces intense shear and energy dissipation in the local region. This highly turbulent zone primarily originates from the piston-like reciprocating motion of the fluid within the moonpool, rapidly converting external flow energy into turbulent energy and dissipating it behind the moonpool [24]. In summary, under 0° incident wave conditions, the distribution characteristics of turbulent kinetic energy, dynamic pressure, and velocity fields all validate the piston effect of the moonpool and its dominant role in the platform's heave response. The numerical results are consistent with the theoretical expectations.

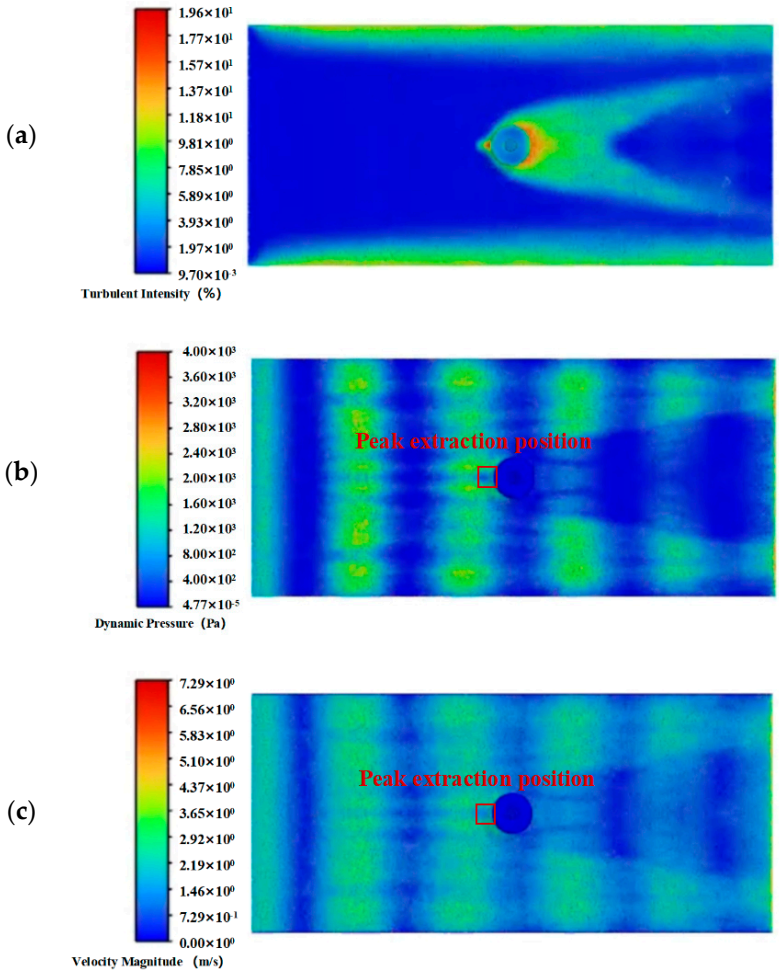


Figure 10. Flow field distribution cloud map around the moonpool platform under 0° wave conditions: (**a**) turbulent kinetic energy, (**b**) dynamic pressure, and (**c**) velocity distribution.

5.4. Analysis of RAO Correction Effectiveness and Damping Coefficient Convergence Characteristics for Platform Heave Motion

Figure 11 shows the comparison of the response amplitude operator (RAO) in the vertical swing direction of the FPSO before and after correction with the literature [16]. The RAO curve before correction exhibited a distinct peak around 16 s, with a maximum value of 7.07 m/m, indicating that the platform experiences severe resonance under this periodic condition according to the potential flow theory results. After viscous damping correction, the peak amplitude in the resonance segment of the RAO curve was significantly reduced to 0.86 m/m. This over-prediction is expected because the standard potential-flow framework does not explicitly account for the viscous dissipation mechanisms associated with moonpool flow. This trend is consistent with the observations in Ref. [8], where incorporating dissipation effectively reduces resonance-induced amplification and improves the stability and reliability of the predicted hydrodynamic response.

Quantitative comparative analysis was conducted between the RAO value curves before and after correction and those in Ref. [16]. Regarding overall forecast accuracy, after correction by the method proposed in this paper, the root mean square error (RMSE) representing the absolute error level decreased from 1.54 to 0.30, a reduction of 80.5%. The mean absolute percentage error (MAPE), reflecting the average relative deviation, decreased from 32.4% to 19.0%, a reduction of 41.4%. These significant improvements in both metrics indicate that the correction strategy effectively enhances forecast accuracy across the entire frequency range.

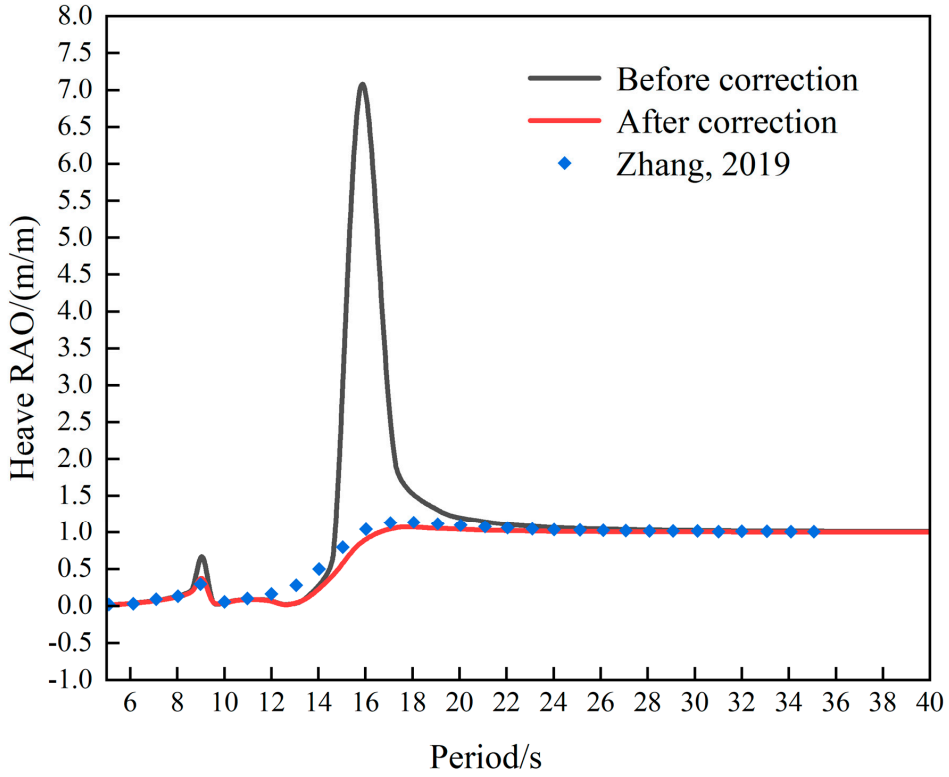


Figure 11. Comparison of RAOs before and after viscous correction for dry tree cylindrical FPSO and literature validation [16].

Regarding critical resonance zone prediction performance, the error between the pre-correction resonance peak RAO and literature values reached 6.28. Post-correction, this error sharply decreased to 0.07, representing a reduction of approximately 98.9%. This demonstrates the method's exceptional correction precision at the peak point exhibiting the most intense motion response, fundamentally rectifying the severe underestimation of resonance responses inherent in traditional potential flow theory. Concurrently, the corresponding period for the RAO peak remained at 11.7 s both before and after correction, perfectly aligning with the incident wave and literature-reported period with zero period shift. This indicates that the correction solely optimized the amplitude response without altering the system's inherent dynamic characteristics, consistent with physical expectations.

In summary, all quantitative metrics consistently demonstrate that the proposed equivalent linearized damping correction method significantly reduces overall prediction errors while preserving the system's correct dynamic characteristics. It achieves highly precise amplitude prediction for the hazardous resonance zone, fully validating its effectiveness and engineering utility in enhancing the reliability of vertical oscillation motion prediction for FPSO units in moonpools.

Figure 12 illustrates the variation of the damping coefficient with the number of correction iterations for incidence angles of 0° and 90°. When the incident wave was 0°, the heave damping coefficient before iteration was 1.633×10^7 N/(m·s). After approximately 2–3 iterations, it rapidly stabilized, ultimately reaching a heave damping coefficient of 1.533×10^7 N/(m·s). Following viscous correction, the damping coefficient decreased by approximately 6.06%. For an incident wave at 90°, the pre-iteration heave damping coefficient was 1.960×10^7 N/(m/s). It exhibited significant variation during the initial iteration phase, gradually decaying as iterations increased. After 5–6 iterations, it converged to a stable level, with the final heave damping coefficient being 2.226×10^7 N/(m·s). After viscous correction, the damping coefficient increased by approximately 13.57%.

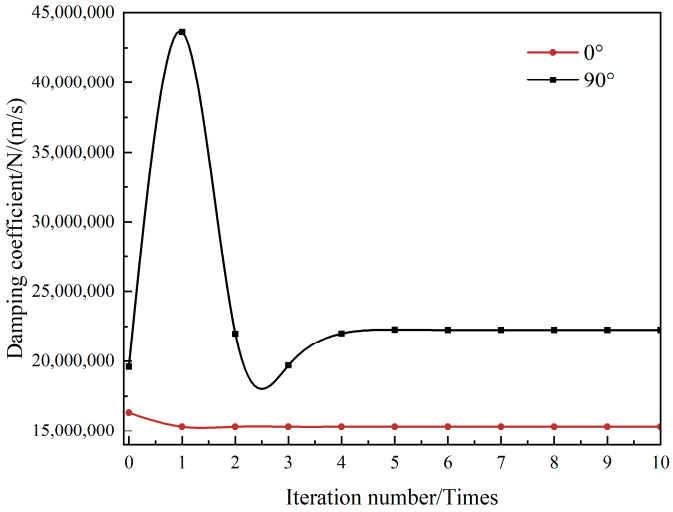


Figure 12. Graph of damping coefficient variation with iteration number for incidence angles of 0° and 90°.

To provide a more universal physical context and enhance result interpretability through dimensionless conversion and literature comparison, this paper converted the dimensioned damping coefficient λ extracted from CFD into a dimensionless damping coefficient C_d based on added mass for analysis. Its calculation formula is [11]:

$$C_d = \frac{\lambda}{\omega M_a} \tag{7}$$

where λ is the dimensioned damping coefficient, ω is the angular frequency of motion, and M_a is the added mass corresponding to the vertical oscillation under the given operating condition. Calculations indicate:

Under the 0° incident wave condition, the added mass M_a is 4.259×10^7 kg; under the 90° incident wave condition, the corresponding added mass M_a is 6.768×10^7 kg), with both exhibiting a dimensionless damping coefficient of 0.67. This result indicates that the system is underdamped and aligns with the dimensionless damping coefficient range reported for similar structures in Ref. [11]. The computational findings are consistent with both engineering experience and theoretical predictions of moonpool hydrodynamics, thereby validating the reliability of the numerical model presented herein.

Significant coupling exists between the floating body motion and the mooring system, with distinct differences observed in the floating body response and maximum cable tension under different wave directions [25]. In this study, the platform mooring system employed a three-point centrally symmetric mooring configuration, resulting in markedly different convergence values for the damping coefficient under the two incident wave conditions. When the incident wave angle was 0°, one mooring group aligned with the wave direction, while the other two groups were symmetrically distributed, resulting in limited damping from the moonpool. Under a 90° wave incidence, the lateral mooring cables experienced stronger excitation, significantly enhancing energy dissipation. Consequently, the final converged damping coefficient was markedly higher than that at 0°. This demonstrates that wave direction significantly influences the damping characteristics of the platform under mooring constraints.

5.5. Comparison of Platform Vertical Oscillation Time-Domain Response and Resistance Before and After Modification

Figure 13 compares the heave response of the platform before and after viscous correction under two wave incidence angles: 0° and 90°. As shown in Figure 13a, the

pre-correction heave response exhibited a large amplitude under 0° incident waves, with the stable segment oscillation amplitude ranging from 4.514 to 6.127 m, demonstrating distinct periodic oscillations. After introducing viscous damping correction, the overall heave response amplitude decreased to 4.743–5.567 m, with significantly reduced oscillation amplitude and peak values. Ref. [15] measured a heave motion amplitude of 0.994 m during a regular wave test under a "once-a-year" design sea state (Hs = 7.2 m, Tp = 11.7 s). After applying the equivalent viscous damping correction method proposed in this paper, the predicted heave motion amplitude decreased significantly from 1.613 m before correction to 0.824 m, representing a reduction of 49%. This result clearly demonstrates that neglecting viscous effects causes potential flow theory to severely underestimate the actual energy dissipation of the system, thereby significantly overestimating the motion response.

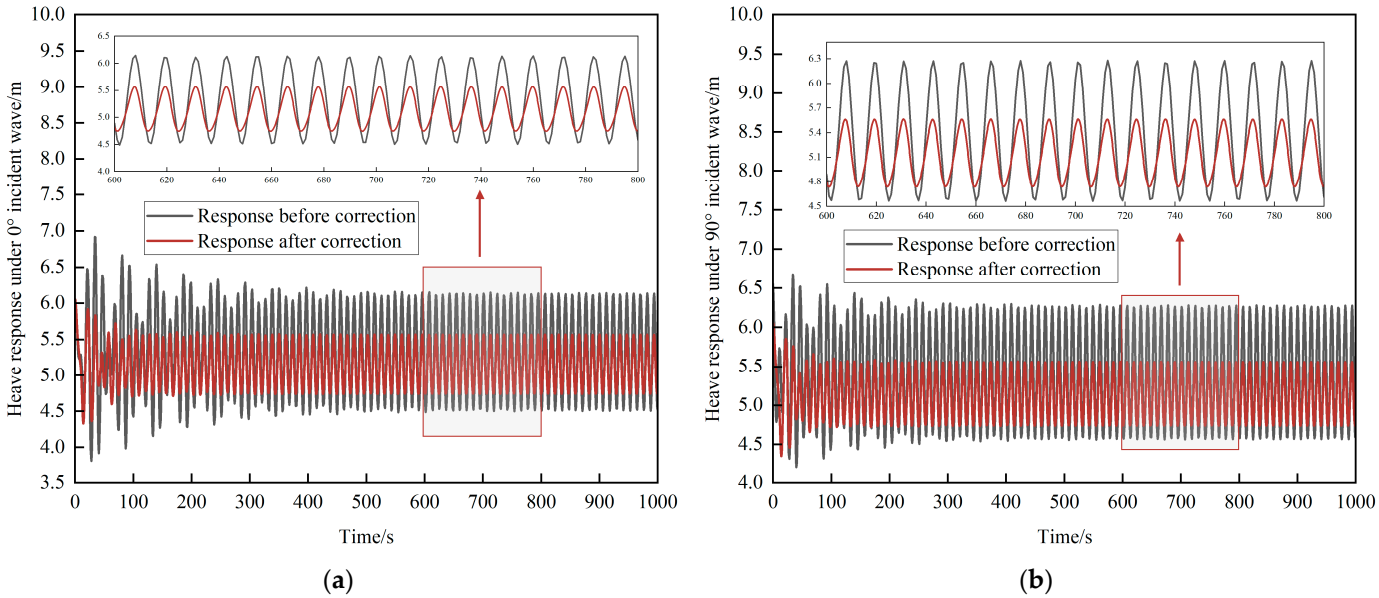


Figure 13. Changes in heave response of the dry tree cylindrical FPSO unit before and after viscous correction under: (**a**) 0° incident wave conditions, and (**b**) 90° incident wave conditions.

The relative deviation between the corrected prediction (0.824 m) and the experimental value from Ref. [15] (0.994 m) was −17.1%. Compared to the +62.6% deviation before correction, this represents a fundamental improvement in prediction accuracy. The corrected amplitude aligns well with results from Ref. [15] under identical wave conditions (once-a-year sea state) and platform scale, further validating the reliability of this method for correcting heave response amplitude.

To validate the universality of the correction method under different wave direction conditions, Figure 13b further illustrates the comparison of the platform's vertical response under a 90° incident wave. As shown, even with altered wave direction, the viscous correction still exhibited significant suppression effects: the uncorrected response features large amplitudes and intense oscillations, with stable-phase oscillation amplitudes ranging from 4.572 to 6.267 m, exhibiting distinct periodic oscillations. The amplitude and peak values of the corrected curve were significantly reduced, with the overall vertical response amplitude decreasing to approximately 4.739–5.560 m and the overall vibration becoming smoother. After applying the proposed equivalent viscous damping correction method, the predicted swing amplitude decreased significantly from 1.695 m before correction to 0.821 m, also achieving a 52% reduction. This demonstrates that the equivalent viscous damping correction method effectively enhances the prediction accuracy of motion responses under different wave directions, further validating its reliability and consistency across various sea conditions.

Figure 14 illustrates the definition of "vertical resistance" as the total hydrodynamic force acting in the vertical (Z-direction) on the platform as a whole, obtained by integrating all wet surface stresses during CFD simulation [26]. This force encompasses the combined contributions of fluid pressure and viscous shear stress. The figure illustrates the time-domain variation of vertical resistance experienced by the platform before and after correction for both 0° and 90° incident directions. When the incident wave angle was 0° (Figure 14a), the uncorrected resistance time-history curve ranged between 3.459×10^8 N and 3.713×10^8 N in the steady-state segment, with an average resistance of approximately 3.586×10^8 N. After viscosity correction, the resistance curve shifted significantly downward overall. The steady-state range narrowed to 3.449×10^8 N to 3.571×10^8 N, with an average resistance of approximately 3.510×10^8 N. The average reduction in resistance before and after correction was approximately 7.6×10^6 N.

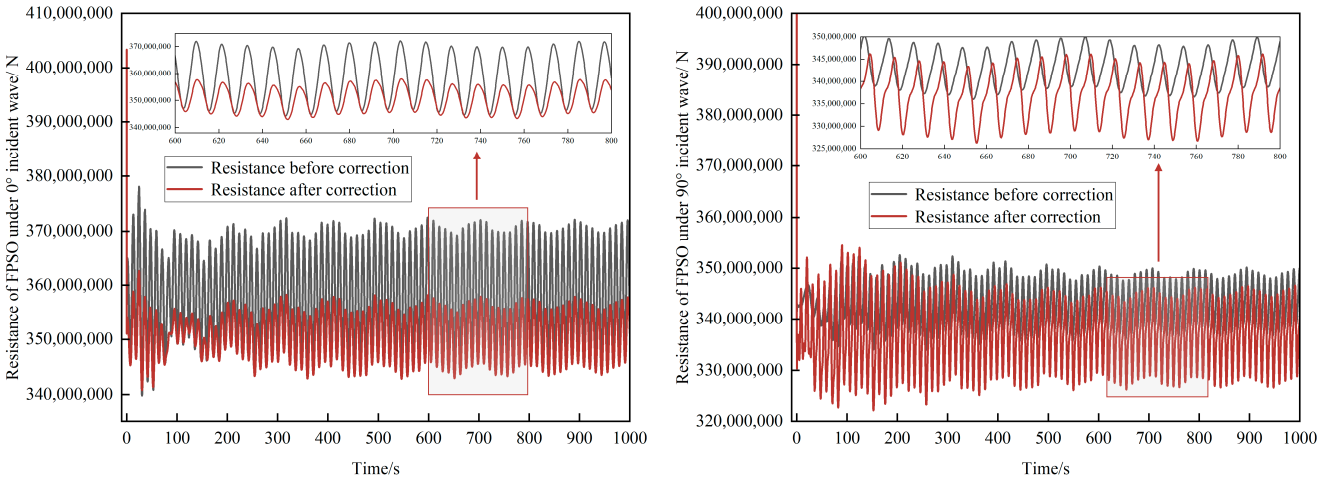


Figure 14. Resistance variation of the dry tree cylinder FPSO unit before and after viscosity correction: (**a**) 0° incident wave conditions, and (**b**) 90° incident wave conditions.

For the 90° incident wave (Figure 14b), the pre-correction stable resistance range was 3.411×10^8 N to 3.495×10^8 N, with an average resistance of approximately 3.453×10^8 N. The corrected curve also shifted downward, with the stable range spanning 3.376×10^8 N to 3.464×10^8 N and an average resistance of approximately 3.420×10^8 N. The average reduction in resistance before and after correction was approximately 3.3×10^6 N. This validates the universality of the viscous damping correction method, which effectively reduces platform hydrodynamic loads under various wave directions.

6. Conclusions

This study implemented and refined an iterative viscous-damping correction framework for the heave response analysis of a cylindrical FPSO unit with a moonpool. Damping identification and motion predictions were performed for both the 0° and 90° incident wave directions, leading to the following conclusions:

(1) Wave monitoring results validate the rationality of numerical wave generation and propagation, indicating that the moonpool effect induces overall reciprocating motion of the internal water mass while attenuating external wave propagation. Flow field distribution characteristics further reveal local energy conversion and dissipation into turbulent energy, demonstrating the significant influence of the moonpool effect on platform heave response.

(2) At a 0° wave direction, the damping coefficient converged rapidly with a final value of 1.533×10^7 N/(m·s). At a 90° wave direction, iterative convergence was slower than at 0° and yielded a higher final value of 2.226×10^7 N/(m/s). The dimensionless damping

coefficient was used to verify the accuracy of the damping results. Both coefficients were 0.67, which is within the range for underdamped systems.

(3) The amplitude of the heave-like time-domain response and resistance was significantly reduced after correction, with smoother curve fluctuations. The results confirm that the iterative approach effectively accounts for the nonlinear dependency of damping on motion amplitude.

This method can be applied in engineering practice for analyzing structures under actual sea conditions, providing a more reliable theoretical basis for FPSO structural design, mooring system configuration, and safe operation assessment. Future research may further explore the effects of irregular waves and different wave height-period combinations on damping effects and investigate the applicability of different moonpool geometries to validate the universality of this method.

Author Contributions: Conceptualization, S.F. and C.A.; Methodology, S.F.; Software, S.F. and Y.X.; Validation, Y.L., T.W. and Y.X.; Formal Analysis, W.G.; Investigation, S.F.; Resources, C.A.; Data Curation, Y.L.; Writing—Original Draft Preparation, S.F.; Writing—Review & Editing, C.A. and W.G.; Visualization, Y.X.; Supervision, C.A.; Project Administration, C.A. All authors have read and agreed to the published version of the manuscript.

Funding: This research received no external funding.

Data Availability Statement: The data presented in this study are available on request from the corresponding author. The data are not publicly available due to project confidentiality.

Conflicts of Interest: Author Shenglei Fu, Wei Gao and Yuanfang Li are employed by the CNOOC Research Institute Co., Ltd. Authors declare no conflict of interests.

References

1. Amin, I.; Dai, S.; Day, S.; Oterkus, S.; Oterkus, E. Experimental investigation on the influence of interceptor plate on the motion performance of a cylindrical FPSO. *Ocean Eng.* **2022**, *243*, 110339. [CrossRef]
2. Deng, S.; Zhong, W.; Yang, X.; Wu, M.; Fu, S. Experimental and numerical study of the hydrodynamic features of a cylindrical FPSO considering current-induced motion. *Ocean Eng.* **2022**, *262*, 112263. [CrossRef]
3. Cui, Y.; Li, Y.; Li, G.; Feng, Y.; Li, H.; Wang, B.; Meng, H.; Deng, W. Dynamic response and nonlinear resonance of cylindrical FPSO with a ring groove considering time-varying restoring stiffness. *Ocean Eng.* **2025**, *325*, 120857. [CrossRef]
4. Zou, L.; Zhao, Z.; Sun, J.; Sun, Z.; Luo, Z.; Yu, Z. Numerical analysis of hydrodynamic characteristics in mooring platforms with diverse moonpool shapes using SPH. *Ocean Eng.* **2024**, *297*, 117037. [CrossRef]
5. Zhao, W.; Yang, X.; Wan, D. Numerical analysis of coupled sloshing and motion of a cylindrical FPSO in regular waves. *J. Hydrodyn. Ser. B* **2024**, *36*, 457–465. [CrossRef]
6. Sanchez-Mondragon, J.; Vázquez-Hernández, A.O.; Cho, S.K.; Sung, H.G. Motion behavior in a turret-moored FPSO caused by piston mode effects in moonpool. *Ocean Eng.* **2017**, *140*, 222–232. [CrossRef]
7. Zhang, Z.; Zhang, H.; Wang, Y.; Zhang, Y. Variation Characteristics of Hydrodynamic Coefficients of Two-Dimensional Rectangular Moonpool Resonance under Sway Motion. *Sustainability* **2022**, *14*, 15952. [CrossRef]
8. Yang, C.; Lu, Z.; Wan, C.; Su, Z.; Bai, X.; Johanning, L. Semi-analytical study on the hydrodynamic performance of a cylindrical moon column FPSO with damping plate. *Ocean Eng.* **2025**, *316*, 119894. [CrossRef]
9. Cui, J.; Chen, X.; Sun, P.; Li, M. Numerical investigation on the hydrodynamic behavior of a floating breakwater with moon pool through a coupling SPH model. *Ocean Eng.* **2022**, *248*, 110849. [CrossRef]
10. *API RP 2SK: Design and Analysis of Stationkeeping Systems for Floating Offshore Structures*, 4th ed.; American Petroleum Institute: Washington, DC, USA, 2024.
11. Ji, X.; Li, Y.; Tang, Y.; Tong, B. Viscous damping effect and vortex shedding performance of the novel anti-motion structures on a cylindrical FPSO. *Ocean Eng.* **2019**, *190*, 106430. [CrossRef]
12. Yu, Y.; Wang, W.; Li, Y.; Liu, L. Influence of periods and amplitudes on damping performance and added mass of cylindrical FPSO. *J. Ocean. Technol.* **2023**, *42*, 112–119.
13. Ding, P.; Xu, R.; Wang, L.; Gao, Z.; Ge, X.; Wen, M. Fractional derivative viscoelastic models based on L2-1σ formula: Modelling and numerical application. *Comput. Geotech.* **2026**, *189*, 107633. [CrossRef]

14. Ponnappan, S.; Sankunny, S. Hydrodynamic Study on Water Column Oscillation of Varying Cross-Sectional Moonpool and Its Effect on Resistance of a Drill Ship. *J. Offshore Mech. Arct. Eng.* **2017**, *140*, 031301. [CrossRef]
15. Lee, S.; Xu, L. *CFD Study and Model Test Verification of Moonpool Configuration Modifications for Minimizing Drillship Resistance*; Springer: Singapore, 2021; pp. 3–27. [CrossRef]
16. Zhang, H. Hydrodynamic Performance Analysis of a Deepwater Cylindrical Drilling Platform in the South China Sea. Master's Thesis, Shanghai Jiao Tong University, Shanghai, China, 2019.
17. Liu, C.; Li, H.; Liu, R.; Zou, J.; Deng, B.; Lu, L. Numerical analysis of FPSO mooring dynamic tension and its fatigue damage under a simplified coupled method considering structural elastic deformation. *Ocean Eng.* **2024**, *314*, 119702. [CrossRef]
18. Rosetti, G.F.; Pinto, M.L.; de Mello, P.C.; Sampaio, C.M.P.; Simos, A.N.; Silva, D.F.C. CFD and experimental assessment of green water events on an FPSO hull section in beam waves. *Mar. Struct.* **2019**, *65*, 154–180. [CrossRef]
19. Lu, S.; Liu, M.; Yang, F.; Zhang, J.; Chen, S.; Liu, L.; Kang, G.; Li, Q. Gas-liquid two-phase flow and mass transfer characteristics in an improved CO_2 wet-wall column. *Chem. Ind. Eng. Prog.* **2023**, *42*, 3457. [CrossRef]
20. Hu, Z.Z.; Yan, S.; Greaves, D.; Mai, T.; Raby, A.; Ma, Q. Investigation of interaction between extreme waves and a moored FPSO using FNPT and CFD solvers. *Ocean Eng.* **2020**, *206*, 107353. [CrossRef]
21. Karpenko, M. Aircraft Hydraulic Drive Energy Losses and Operation Delay Associated with the Pipeline and Fitting Connections. *Aviation* **2024**, *28*, 1–8. [CrossRef]
22. Huo, S.; Deng, S.; Song, Z.; Zhao, W.; Wan, D. On the hydrodynamic response and slamming impact of a cylindrical FPSO in combined wave-current flows. *Ocean Eng.* **2023**, *275*, 114139. [CrossRef]
23. Li, Y.; Cai, M.; Zhang, C.; Law, Y.Z.; Zhang, S.; Santo, H. Load mapping technology in floating offshore structures: A frequency-domain methodology for coupled hydro-structure analysis of FPSO with a large number of liquid tanks. *Eng. Struct.* **2026**, *349*, 121853. [CrossRef]
24. Wei, Q.; Gu, J.; Liu, W.; Lyu, H.; Tao, Y.; Hu, F. Influence of an Adding Damping Device in a Moonpool on the Heave Motion of a Drilling Ship Part I: Experiment. *China Ocean Eng.* **2025**, *39*, 191–208. [CrossRef]
25. Guo, X.; Lu, H.; Yang, J.; Peng, T. Resonant water motions within a recessing type moonpool in a drilling vessel. *Ocean Eng.* **2017**, *129*, 228–239. [CrossRef]
26. Wang, G.; Zhang, J.; Lu, B.; Lin, X.; Wang, F.; Liu, S. Experimental investigation of motion response and mooring load of semi-submersible tidal stream energy turbine under wave-current interactions. *Ocean Eng.* **2024**, *300*, 117445. [CrossRef]

Disclaimer/Publisher's Note: The statements, opinions and data contained in all publications are solely those of the individual author(s) and contributor(s) and not of MDPI and/or the editor(s). MDPI and/or the editor(s) disclaim responsibility for any injury to people or property resulting from any ideas, methods, instructions or products referred to in the content.